

Zinc-Triazolate Metal-Organic Framework Assisted Synthesis of Germanium Nanoparticles Encapsulated in Nitrogen-Doped Carbon as Anode Materials for Lithium-Ion Batteries

Zhuo Wang,^[a, b] Xue Bai,^[a] Jiabao Dong,^[a] Kexin Zhang,^[a] Bin Zhao,^{*[a]} and Xiaoli Dong^{*[b]}

Germanium (Ge) is demonstrated to be prospective as a lithium-ion battery anode material, yet the cycling stability is undermined by substantial volume fluctuations, restricting its viability for practical applications. Here, we present a facile Zn-based metal–organic framework (MOF) engaged route to produce Ge nanoparticles *in situ* encapsulated in nitrogen-doped mesoporous carbon (denoted as Ge@N-C) as an anode material. This method uses a zinc-triazolate MOF (MET-6) and commercial GeO₂ as the hybrid carbon and Ge precursors. After a heating treatment, the Ge@N-C composite is readily obtained

along with the simultaneous thermal decomposition of MET-6 and the reduction of GeO₂. Benefiting from the mesoporous structure and high electrical conductivity of N-C, along with the strong interaction between Ge and N-C, the obtained Ge@N-C electrode exhibits a significant reversible charge capacity of 1012.8 mAh g⁻¹ after 150 cycles at 0.1 A g⁻¹, and excellent rate capability. Furthermore, a reversible charge capacity of 521.1 mAh g⁻¹ can be maintained at 5.0 A g⁻¹ after 1000 cycles.

Introduction

Lithium-ion rechargeable batteries (LIBs) have significant potential for electrochemical energy storage due to their high energy density and long-term cycling stability.^[1–3] They are extensively utilized in a variety of devices such as portable electronic gadgets, electric cars, and other similar products. However, the typical commercial anode material, graphite, is far from satisfying the rapidly growing demand for high-performance energy storage devices due to its low theoretical lithium storage capacity (372 mAh g⁻¹).^[4–6] Therefore, developing alternative high-capacity anode materials is urgently required to enhance the performance of LIBs.

Group IVA non-carbon elements, particularly silicon (Si) and germanium (Ge), are considered promising alternative anode active materials to replace the existing graphite for next-generation LIBs, attributed to their high theoretical specific capacity (4200 mAh g⁻¹ for Si and 1600 mAh g⁻¹ for Ge).^[7–9] In contrast to Si, Ge features superior intrinsic electrical conductivity (104 times higher) and faster lithium-ion diffusivity (400 times faster at room temperature).^[10,11] These characteristics

make Ge a more appealing anode candidate for high-power LIBs. Nevertheless, akin to the case of silicon, the practical implementation of pure elemental Ge as an anode active material is hindered by significant volume fluctuations during Li⁺ insertion and extraction. These fluctuations can result in pulverization issues, causing a loss of electrical connectivity between the Ge anode material and the current collector, ultimately leading to swift capacity deterioration.^[12,13] To alleviate this issue, significant recent research efforts have focused on exploiting Ge-based materials capable of accommodating the large volume change, including fabricating nanosized Ge with various morphologies (e.g., nanoparticles, nanowires, nanotubes),^[14–16] constructing porous Ge,^[17–20] and developing composites with conductive carbon matrices.^[21–23] The nanosized Ge can mitigate the stress-induced structural alterations and shorten the lithium ion diffusion distance, thus achieving higher capacity and better cycling stability relative to their bulk counterparts. However, the inevitable agglomeration of Ge nanoparticles during repeated cycling usually leads to insufficient cycling life and poor rate capability. Constructing composite structures by integrating nanostructured Ge with carbon materials has been regarded as an effective approach for addressing the aforementioned issues. In this regard, various carbon-based materials have been applied to prepare such composites, such as amorphous carbon,^[24–28] graphene,^[29–32] carbon nanotubes,^[33,34] and their hybrid materials.^[35–37] Since these carbon matrices serve to boost electronic conductivity of the composite, while also function as a buffer layer to accommodate the volume changes and inhibit Ge particles from agglomerating, the resultant composite electrodes show significantly improved electrochemical properties. Furthermore, the nitrogen-doped carbon composites have been demonstrated to significantly enhance the lithium storage properties

[a] Z. Wang, X. Bai, J. Dong, K. Zhang, B. Zhao
School of Materials and Chemistry, University of Shanghai for Science and Technology, No. 516 Jungong Road, Shanghai 200093, China
E-mail: zhaobin@usst.edu.cn

[b] Z. Wang, X. Dong
Department of Chemistry and Shanghai Key Laboratory of Molecular Catalysis and Innovative Materials, Institute of New Energy, iChEM (Collaborative Innovation Center of Chemistry for Energy Materials), Fudan University, No. 2005 Songhu Road, Shanghai 200433, China
E-mail: xldong@fudan.edu.cn

 Supporting information for this article is available on the WWW under <https://doi.org/10.1002/batt.202400442>

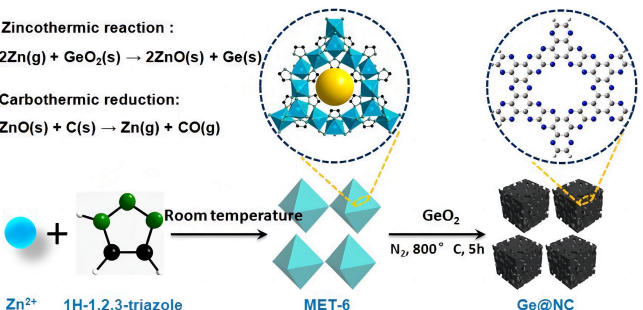
by boosting the electronic conductivity. Unfortunately, most of the reported nanoscale Ge/carbon composites are synthesized using expensive Ge precursors (such as $C_{12}H_{10}Ge$, $GeCl_4$, and GeI_2) through multiple complicated steps. In addition, the weak interaction between Ge and carbon matrix is not sufficient to hold the structure integrity of the active material upon cycling, resulting in unsatisfactory electrochemical performance.^[31,32] Thus, the development of a simple method to fabricate Ge/carbon materials with good cyclability is highly desirable.

Metal-organic frameworks (MOFs) are increasingly popular as functional materials due to their diverse chemical compositions, large surface areas, and regular porous structures. To date, a variety of carbon-based nanostructured porous materials have been successfully fabricated by using MOFs as precursors and/or templates.^[36,37] Nevertheless, only one work has been made toward the preparation of Ge/carbon anode material from MOFs. Lee et al. reported the synthesis of Ge/carbon using $Zn(adipate)(phen)(H_2O)$ as a precursor, demonstrating a specific capacity of about 600 mAh g^{-1} after 300 cycles at 0.5°C .^[37] There has been no previous relevant report regarding the synthesis of germanium/nitrogen-doped carbon composites derived from MOFs. It is therefore of great interest to explore suitable MOFs to construct Ge-based anode materials with enhanced performance.

Herein, we present a novel MOF-engaged approach to the germanium nanoparticles *in situ* encapsulated in nitrogen-doped mesoporous carbon (Ge@N-C) anode for high stability LIB. In this method, a Zn-rich MOF with nitrogen-containing organic ligands, zinc-triazolate framework (MET-6), is selected as reaction media due to its good thermal stability and facile large-scale preparation at room temperature, and the cost-effective GeO_2 is used as the Ge precursor. The Ge@N-C composite is readily obtained by one-step carbonization of the mixture of MET-6 and GeO_2 at 800°C under N_2 atmosphere. During the carbonization process, the Zn nodes in MET-6 are thermally reduced to metallic Zn nanoparticles, followed by the simultaneous zincothermic reduction of GeO_2 to Ge and ZnO . Meanwhile, the triazole ligands are transformed into N-doped carbon matrix, which *in situ* encapsulates the as-formed Ge nanoparticles and reacts with ZnO to yield metallic Zn by the carbothermic reduction reaction, thereby leading to the formation of Ge@N-C composite. This procedure creates the strong interaction between Ge and N–C matrix. Moreover, the mesoporous structure is generated in the N-doped carbon matrix because of the decomposition of triazole ligands and the evaporation of metallic Zn. As a result of this unique structure, the obtained Ge@N-C exhibits large reversible capacity, and long-term cycling stability when employed as a LIBs anode material.

Results and Discussion

The preparation process of Ge@N-C is illustrated in Scheme 1. First, octahedral Zn-containing MOF ($Zn(C_2H_2N_3)_2$) crystals with a particle size of 200 nm were synthesized on the basis of a previous report via the coordination reaction between 1H-1,2,3-



Scheme 1. Schematic illustration of the preparation process of Ge@N-C.

triazole and zinc chloride at room temperature (Figure S1).^[36] The XRD pattern (Figure S2) of this MOF matches well with previous reports, suggesting the high purity of the as-synthesized $Zn(C_2H_2N_3)_2$ crystallites. Subsequently, Ge@N-C was obtained by heat treatment of a stoichiometric mixture of the as-prepared $Zn(C_2H_2N_3)_2$ and commercial GeO_2 (molar ratio of Zn^{2+} : $Ge^{4+} = 2:1$) at 800°C under N_2 atmosphere, without any further acid washing.

The SEM image in Figure 1a shows that Ge particles with sizes of about 200–300 nm are anchored on the MOF-derived nitrogen-doped porous carbon framework. The TEM image (Figure 1b) displays that Ge particles are encapsulated in porous carbon matrix. The HRTEM image (Figure 1c) also confirms the existence of carbon and metallic Ge in the composite. The lattice fringes with interplanar distances of 0.20 and 0.34 nm correspond well with the (220) plane of metallic Ge particles and the (002) plane of graphitic carbon, respectively. Furthermore, the chemical mappings (Figure 1d) demonstrate that the elements Ge, C, N, and O are well-distributed within the sampled area. The presence of elemental oxygen comes from the adsorbed O_2 on the surface of the sample. The elemental analysis in Table S1 further verifies the C content.

The formation of Ge@N-C was confirmed by the XRD analysis. The Rietveld refinement XRD result (Figure 2a) shows that the diffraction peaks are well matched to the cubic phase Ge crystalline (JCPDS no. 04-0545; space group $Fd\bar{3}\,m$, $a = 5.657 \text{ \AA}$), suggesting that GeO_2 has been successfully converted into crystalline Ge through the zincothermic reduction process, which is represented by the chemical equation: $2Zn(g) + GeO_2(s) \rightarrow 2ZnO(s) + Ge(s)$.^[18] Interestingly, no peaks corresponding to the ZnO byproducts are observed, indicating that ZnO is reduced to Zn metal through carbothermic reduction ($ZnO(s) + C(s) \rightarrow Zn(g) + CO(g)$), and then removed by evaporation. Rietveld refinement of powder XRD patterns is shown in Table S2. This phenomenon has been previously observed for a Ge/carbon composite prepared by Lee et al.^[37] The carbon (002) plane diffraction peak is not detected in the XRD pattern, possibly caused by the strong diffraction intensity of Ge. To confirm the presence of carbon, Raman characterization was performed, with results displayed in Figure 2b. A sharp peak at 285 cm^{-1} corresponds to the stretching vibration mode of Ge–Ge bonding. The three peaks at 1335, 1588, and 2834 cm^{-1} represent the D, G, and 2D bands of carbon, respectively.^[31] The

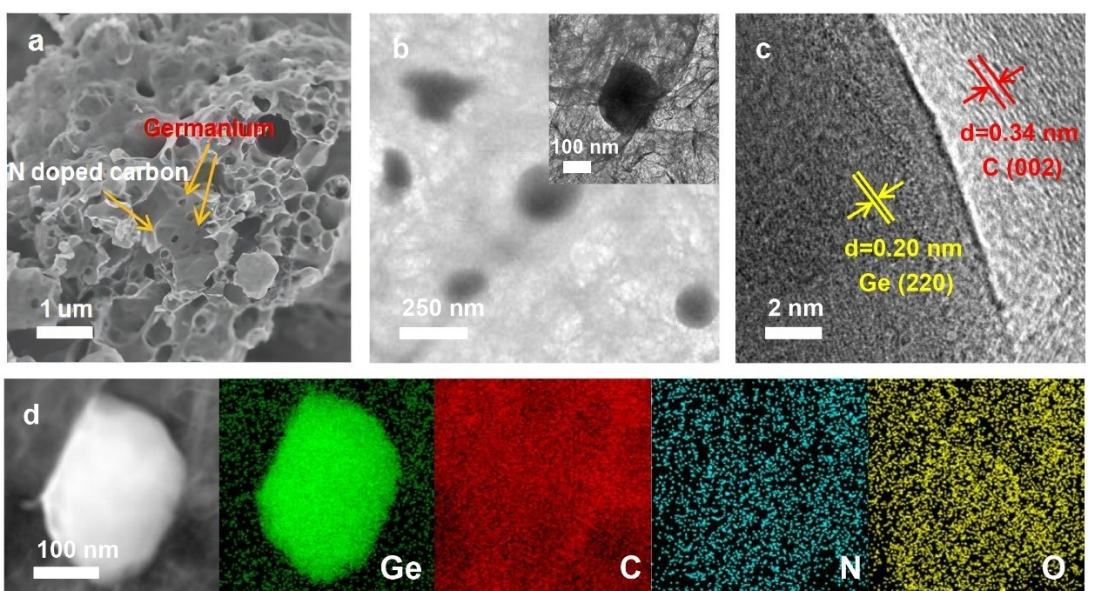


Figure 1. (a) SEM, (b) TEM (the inset is the magnified TEM image), (c) HRTEM, and (d) the corresponding EDS mapping images of the as-prepared Ge@N-C.

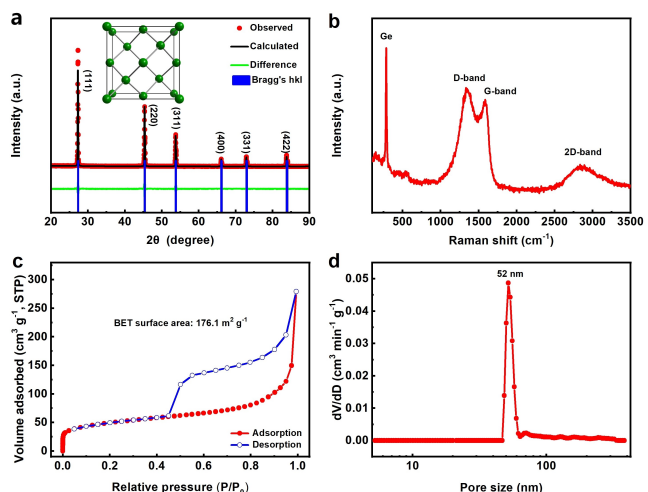


Figure 2. (a) XRD pattern, (b) Raman spectrum, (c) nitrogen adsorption-desorption isotherms, and (d) pore size distribution plot of the as-prepared Ge@N-C.

intensity of the D band exceeds that of the G band, implying the abundant defects and a disordered carbon structure after N doping in the Ge@N-C material. The presence of the single-peak 2D band in Raman spectroscopy also suggests that carbon in Ge@N-C offers good conductivity.

The porous nature of Ge@N-C was examined through the N_2 adsorption-desorption method. The isotherm of Ge@N-C (Figure 2c) depicts a type-IV curve with a noticeable hysteresis loop ($0.45 < P/P_0 < 1$). The specific surface area and pore volume are calculated as $176.1 \text{ m}^2 \text{ g}^{-1}$ and $0.292 \text{ cm}^3 \text{ g}^{-1}$, respectively. The simulated pore size distribution using the nonlocal density functional theory (Figure 2d) reveals a mesoporous structure centred at 52 nm. Such a mesoporous configuration effectively enhances lithium-ion diffusion and mitigates mechanical stress.

To further obtain insight into the chemical composition in Ge@N-C, XPS analysis was conducted. The survey spectrum of Ge@N-C in Figure 3a indicates the existence of Ge, C, N, and O in the sample. The Ge 3d spectrum (Figure 3b) displays four peaks at 29.6, 30.6, 31.5, and 33.1 eV, which are ascribed to Ge–Ge, Ge–C, Ge–N, and Ge–O bonds, respectively.^[28] The presence of Ge–O bonds might be due to the surface oxidation of Ge. The C 1s spectrum (Figure 3c) could be deconvoluted into five distinct peaks. It is possible to identify the peaks of C–Ge (284.1 eV), C=C (284.6 eV), C–N (285.5 eV), C–O (286.3 eV), and C=O (287.2 eV) in the spectrum.^[22] The High-resolution N 1s spectrum (Figure 3d) can be fitted into three characteristic peaks, assigning to Ge–N (397.7 eV), pyridinic N (398.8 eV), and pyrrolic N (400.7 eV), indicating a nitrogen doped carbon matrix generated from the triazole linker of MOF upon carbonization.^[35] The incorporation of nitrogen in porous carbon matrix enhances electrical conductivity and provides more active sites for lithium storage, which is favourable for improving the performance of electrochemical lithium storage, improving the lithium storage properties.

The electrochemical behaviour of Ge@N-C in rechargeable LIBs was evaluated in CR2016 coin cells. Figure 4a shows the cyclic voltammetry (CV) profiles of the first three cycles at 0.1 mV s^{-1} . In the initial cathodic process, a single reduction peak emerges at 0.24 V, however, it diminishes in the subsequent cycles, indicating the development of a solid electrolyte interphase (SEI) layer. The peak located at about 0.44 V stems from the reduction of Ge. This peak is divided into two peaks at 0.37 V and 0.48 V in the subsequent two cycles, indicating the formation of distinct Li_xGe alloys. Two oxidation peaks at 0.38 and 0.58 V were measured during the initial anodic process, correlating with the delithiation reaction of Li_xGe , consistent with the previous report.^[10] After the first cycle, CV curves are nearly overlapped, indicating the highly reversible nature of the

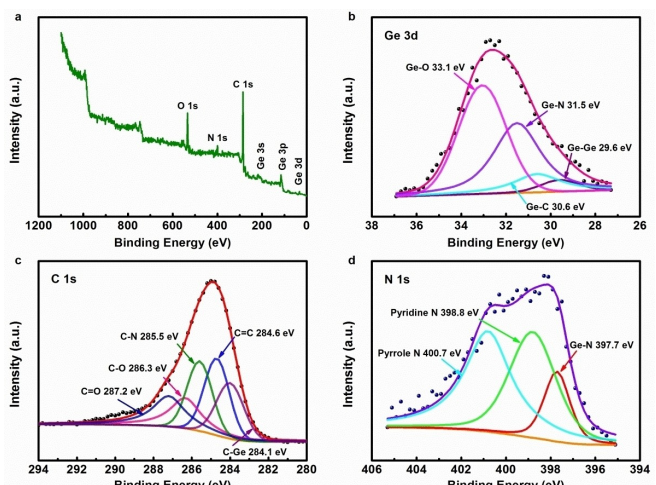


Figure 3. XPS spectra of Ge@N-C. (a) the survey spectrum and the high-resolution spectra for (b) Ge 3d, (c) C 1s, and (d) N 1s.

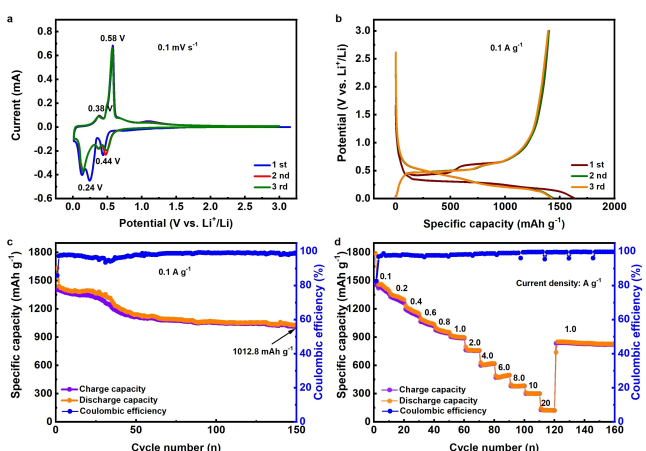


Figure 4. Electrochemical performance of Ge@N-C as anode material for LIBs. (a) Cyclic voltammetry (CV) profiles of the first three cycles at a scan rate of 0.1 mV s^{-1} between 0.01 and 3.0 V versus Li/Li^+ . (b) Galvanostatic discharge/charge curves at a current density of 0.1 A g^{-1} . (c) Cycling performance at a current density of 0.1 A g^{-1} . (d) Rate capability of Ge@N-C anode at different current densities.

Ge@N-C anode. The initial three galvanostatic discharge/charge curves of the Ge@N-C anode measured at 0.1 A g^{-1} are depicted in Figure 4b. The first discharge and charge capacities are 1631.7 and $1400.3 \text{ mAh g}^{-1}$, with an initial Coulombic efficiency of 85.8% . The 14.2% capacity loss occurring during the first cycle is mainly due to the presence of SEI layer on the Ge@N-C electrode surface. In the following two cycles, the charge capacities of 1400.3 and $1392.3 \text{ mAh g}^{-1}$ are obtained with high Coulombic efficiencies of 97.3% and 97.8% , demonstrating the high reversibility of the Ge@N-C anode. The cycling performance of Ge@N-C anode at 0.1 A g^{-1} is illustrated in Figure 4c. The charge capacity decreases slowly to $1284.1 \text{ mAh g}^{-1}$ after 30 cycles (91.7% of the first charge capacity), then the capacity is stabilized and retained at $1012.8 \text{ mAh g}^{-1}$ after 150 cycles (72.3% of the first charge capacity) with a corresponding Coulombic efficiency greater than 98.7% , indicating an excel-

lent cycling stability. The rate capability of the Ge@N-C anode was examined at different current densities ranging from 0.1 to 20 A g^{-1} for every 10 cycles (Figure 4d). The average charge capacities are 1437.3 , 1300.9 , 1156.6 , 1041.3 , 953.2 , 894.3 , 758.4 , 608.3 , 480.2 , and 377.8 mAh g^{-1} at various current densities. At a high current density of 10 A g^{-1} , the electrode maintains a charge capacity of 299.7 mAh g^{-1} . Reverting to 1.0 A g^{-1} after 120 cycles, an average charge capacity as high as 840.2 mAh g^{-1} is recovered, demonstrating exceptional rate performance. The corresponding voltage profile at different current densities is illustrated in Figure S3.

The Ge@N-C and commercial Ge particles were used for performance comparison at 1.0 A g^{-1} (Figure 5a). The pure Ge anode delivers a relatively large initial charge capacity of $1447.4 \text{ mAh g}^{-1}$, but its reversible capacity declines rapidly to only 280.2 mAh g^{-1} after 50 cycles, indicating a significant capacity reduction of 80.6% . The poor cycle performance for the pure Ge anode is due to the severe volume changes during cycling, leading to the pulverization and electrical disconnection between particles. In contrast, Ge@N-C displays a significantly improved cycling stability. The Ge@N-C exhibits a charge capacity of 777.8 mAh g^{-1} initially, which decreases to 710.5 mAh g^{-1} by the 50 th cycle. Even after 500 cycles, it maintains a charge capacity of 650.0 mAh g^{-1} , showcasing an impressive 83.6% high-capacity retention. We also investigated the capacity contribution of nitrogen-doped porous carbon derived from MET-6 (Figure S4). Figure S5 illustrates the electrochemical performance of Ge@N-C electrodes at loading masses of 1.5 , 2.0 , and 2.5 mg cm^{-2} . Notably, the electrode with 2.5 mg cm^{-2} achieves a specific capacity of 779.3 mAh g^{-1} , indicating that Ge@N-C electrodes with higher mass loadings can be effectively used in batteries. Furthermore, SEM images of the Ge@N-C electrode at various cycling stages show no significant electrode fracture (Figure S6), suggesting a stable electrode structure throughout the cycling processes. The enhanced electrochemical performance of Ge@N-C can be attributed to the existence of nitrogen-doped porous carbon coating layer. This particular coating boosts conductivity, while also offering ample room for accommodating volume fluctuations, thereby improving the stability of the anode significantly. As shown in Figure 5b, the Ge@N-C electrode is first activated at a low current density of 0.5 A g^{-1} for three cycles followed by cycling at 5.0 A g^{-1} . The discharge and charge capacities for the first cycle at 5.0 A g^{-1} are 978.8 and 956.3 mAh g^{-1} , respectively. After 1000 cycles, it can retain a charge capacity of 521.1 mAh g^{-1} with a low-capacity decay of 0.046% per cycle, surpassing many previously reported Ge-based anode materials for LIRBs (Table S3).

The electrochemical kinetics of Ge@N-C electrodes were explored via scanning CV curves at various scan rates. As shown in Figure S7(a), the CV curves obtained at different scan rates are similar in shape. Normally, the current (i) of CVs obeys a power-law relationship with the scan rate (v) that is described by $i = av^b$, where a and b are the adjustable parameters. The b value indicates the slope of the $\log(i)$ vs $\log(v)$ curve. Typically, $b=0.5$ represents a diffusion-controlled process, whereas $b=1.0$ signifies capacitive behavior.^[17] Figure S7b shows the

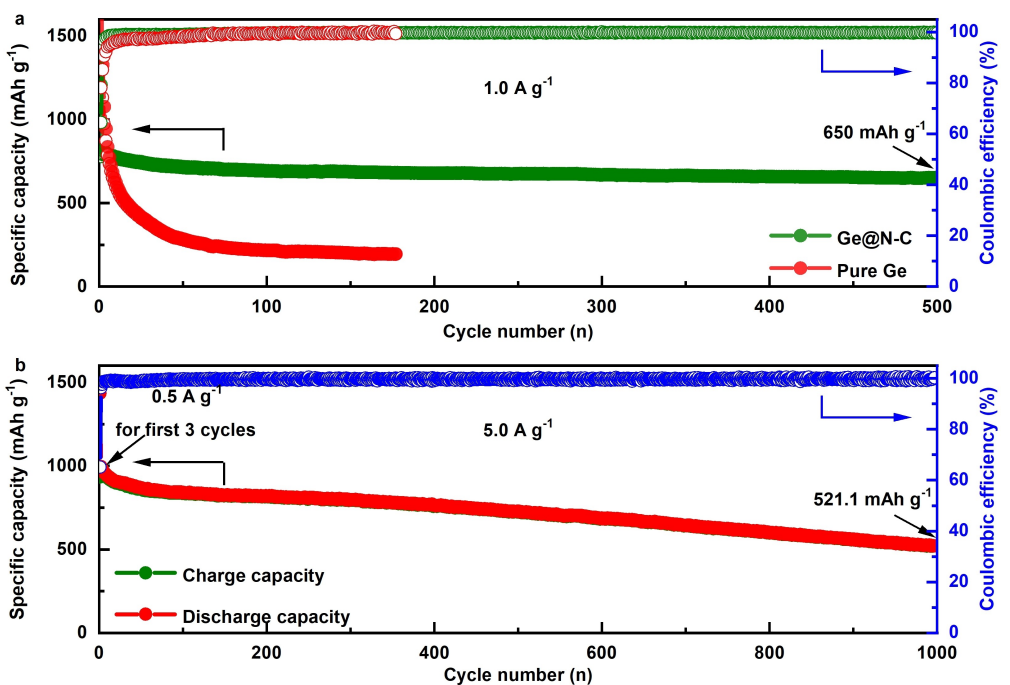


Figure 5. (a) The cycling performance comparison of Ge@N-C and commercial pure Ge electrodes at 1.0 A g⁻¹. (b) Cycling performance and the corresponding Coulombic efficiency of the Ge@N-C electrode at 5.0 A g⁻¹.

calculated b-values for anodic and cathodic peaks are 0.6885, 0.7270, 0.7717, and 0.7622, suggesting that the electrochemical reaction in the Ge@N-C cell is controlled by both diffusion and capacitive processes. Moreover, the capacitive contribution can be calculated using the formula: $i = k_1v + k_2v^{1/2}$, where k_1v and $k_2v^{1/2}$ symbolize the capacitive- and diffusion-controlled proportions, respectively.^[35] As shown in the shaded area (Figure S7c), the capacitive-controlled contribution is 41.2% at 0.2 mV s⁻¹. As the scanning rate rises, the capacitive contribution percentage grows, reaching 80% at 6.0 mV s⁻¹ (Figure S7d), indicating the favorable charge-transfer kinetics of the Ge@N-C electrode. As Figure S8 shows, the kinetic performance of the lithium-ion diffusion was further investigated by the galvanostatic intermittent titration (GITT). Figure S8a presents the 2nd charge/discharge curve of voltage variation with galvanostatic pulses, which consists of a series of pulses, galvanostatic and of relaxation. Each step involved using a 100 mA g⁻¹ pulse current for 20 minutes, followed by a two-hour standing period. (Figure S8b). According to Fick's second law of diffusion, the calculated $\lg D_{Li^+}$ values are between -11 and -13 during discharge, while they vary in the range of -11 to -15 during charge processes (Figures S8c-d). In this case, the presence of $\lg D_{Li^+}$ minima could arise from phase transitions or ordered-disordered transitions during cycling. Figure S9 shows electrochemical impedance spectroscopy (EIS) measurements carried out on the Ge@N-C electrode before and after 50 cycles. All curves consist of semicircles and straight lines corresponding to interfacial charge transfer resistance (R_{ct}) and ion diffusion, respectively. The R_{ct} after 50 cycles (12.8 Ω) is significantly lower than that of the initial state (199 Ω), indicating a lower interfacial charge transfer impedance. A steeper slope of the

electrode (after 50 cycles) in the low-frequency region also indicates improved Li⁺ diffusion performance.

Exploring further the lithium-ion storage mechanism of Ge@N-C, Figure 6 and Figure S10 illustrate the in-situ XRD patterns obtained on cycling. Significantly, there are some unaffected peaks corresponding to Be (50.86°, 52.74°), BeO (38.48°, 41.20°, and 43.84°) in the beryllium window, and Cu foil (43.24°, 50.38°), respectively, in the in-situ XRD-measured battery testing setup. Upon discharge to 0.44 V, the peaks related to the (111), (220), and (311) crystal planes of Ge shift to a lower angle with an increased half-peak width, possibly due to the insertion of the lithium ion.^[33] The Li₁₅Ge₄ signal peak appears when it approaches the fully discharged state at 0.11 V. While in the charge process, this peak gradually weakens and eventually disappears, revealing the amorphous processes. However, in the subsequent discharge, the peak intensity of Li₁₅Ge₄ gradually increases. These findings indicate that the transition from amorphous to crystalline in Ge@N-C is reversible throughout the cycling processes.

Conclusions

In summary, Ge@N-C composite with Ge nanoparticles encapsulated in nitrogen-doped mesoporous carbon has been successfully prepared via a Zn-based MOF engaged strategy and applied as an anode in lithium-ion batteries. The synthetic process involves the simultaneous thermal decomposition of Zn-based MOF and the reduction of GeO₂. Due to the high dispersion, large surface area, and enhanced conductivity of the carbon coating, coupled with the strong interaction between

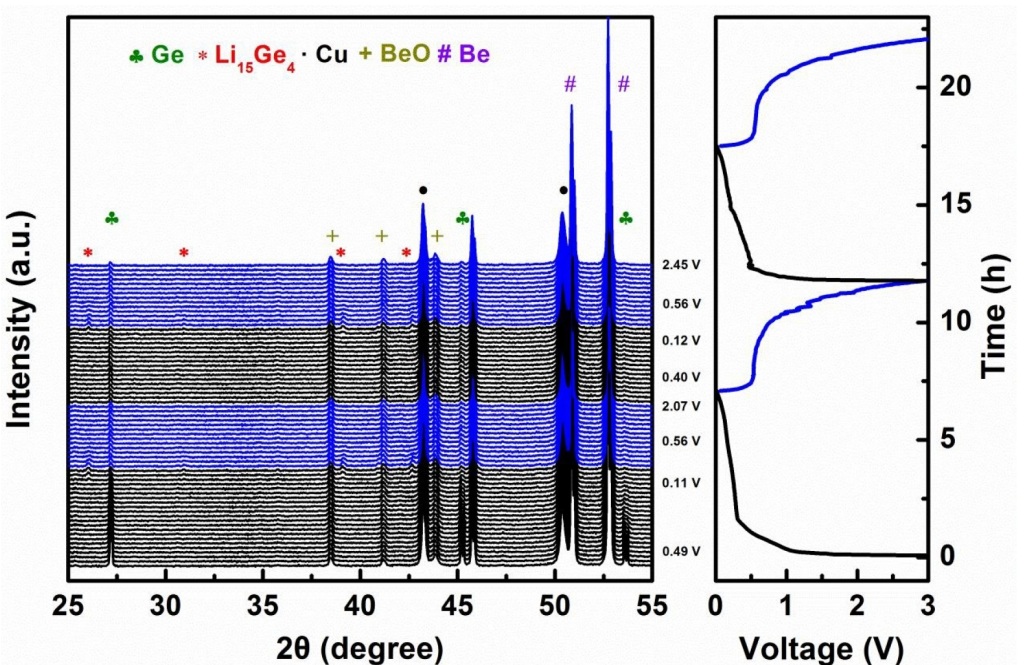


Figure 6. In-situ XRD pattern of Ge@C-N electrode.

Ge and N-C, the Ge@N-C composites obtained exhibited a capacity of 650 mAh g^{-1} after 500 cycles at 1.0 A g^{-1} and exceptional high-rate performance. Even after 1000 cycles at 5 A g^{-1} , a consistent capacity of 521.1 mAh g^{-1} can still be maintained. The innovative synthesis method can be further developed to produce more high-performance anode materials in energy storage devices.

Acknowledgements

The authors appreciate the funding support of the National Natural Science Foundation of China (22209114), Chenguang Program of Shanghai Education Development Foundation and Shanghai Municipal Education Commission (21CGA56).

Conflict of Interests

The authors declare no conflict of interest.

Data Availability Statement

The data that support the findings of this study are available in the supplementary material of this article.

Keywords: Germanium • Metal-organic framework • Nitrogen-doped mesoporous carbon • Anode materials • Lithium-ion batteries

- [1] R. V. Noorden, *Nature* **2014**, *507*, 26–28.
- [2] X. Min, G. Xu, B. Xie, P. Guan, M. Sun, G. Cui, *Energy Storage Mater.* **2022**, *47*, 297–318.
- [3] L. Ji, Z. Lin, M. Alcoutlabi, X. Zhang, *Energy Environ. Sci.* **2011**, *4*, 2682–2699.
- [4] C. Zhu, J. Mao, J. Zhao, Y. Luo, J. Li, C. Lei, G. Li, F. Cheng, *Adv. Funct. Mater.* **2024**, *2406730*, DOI: 10.1002/adfm.202406730.
- [5] P. Liu, B. Li, J. Zhang, H. Jiang, Z. Su, C. Lai, *Chin. Chem. Lett.* **2023**, *34*, 107946.
- [6] T. Wang, J. Sha, W. Wang, Y. Ji, Z.-M. Zhang, *Chin. Chem. Lett.* **2023**, *34*, 107929.
- [7] D. Liu, Z. Liu, X. Li, W. Xie, Q. Wang, Q. Liu, Y. Fu, D. He, *Small* **2017**, *13*, 1702000.
- [8] A. K. Prajapati, A. Bhatnagar, *J. Energy Chem.* **2023**, *83*, 509–540.
- [9] Y. Chen, Y. Zou, X. Shen, J. Qiu, J. Lian, J. Pu, S. Li, F.-H. Du, S.-Q. Li, Z. Ji, A. Yuan, *J. Energy Chem.* **2022**, *69*, 161–173.
- [10] X. Liu, X.-Y. Wu, B. Chang, K.-X. Wang, *Energy Storage Mater.* **2020**, *30*, 146–169.
- [11] X. Fang, C. Jiang, C. Yue, F. Hu, *Chem. Eur. J.* **2024**, *30*, e202400063.
- [12] H. Lee, M. G. Kim, C. H. Choi, Y.-K. Sun, C. S. Yoon, *J. Phys. Chem. B* **2005**, *109*, 20719–20723.
- [13] T. Kennedy, E. Mullane, H. Geaney, M. Osiak, C. O'Dwyer, K. M. Ryan, *Nano Lett.* **2014**, *14*, 716–723.
- [14] M.-H. Park, Y. Cho, K. Kim, J. Kim, M. Liu, J. Cho, *Angew. Chem. Int. Ed.* **2011**, *123*, 9821–9824.
- [15] M.-H. Park, K. Kim, J. Kim, J. Cho, *Adv. Mater.* **2010**, *22*, 415–418.
- [16] S. Choi, J. Kim, N.-S. Choi, M. G. Kim, S. Park, *ACS Nano* **2015**, *9*, 2203–2212.
- [17] C. Kim, G. Song, L. Luo, J. Y. Cheong, S.-H. Cho, D. Kwon, S. Choi, J.-W. Jung, C.-M. Wang, I.-D. Kim, S. Park, *ACS Nano* **2018**, *2*, 8169–8176.
- [18] N. Lin, T. Li, Y. Han, Q. Zhang, T. Xu, Y. Qian, *ACS Appl. Mater. Interfaces* **2018**, *10*, 8399–8404.
- [19] D. T. Ngo, H. T. Le, C. Kim, J.-Y. Lee, J. G. Fisher, I.-D. Kim, C.-J. Park, *Energy Environ. Sci.* **2015**, *8*, 3577–3588.
- [20] Y. Wang, S. Luo, M. Chen, L. Wu, *Adv. Funct. Mater.* **2020**, *30*, 2000373.
- [21] J. Liang, X. Li, Z. Hou, T. Zhang, Y. Zhu, X. Yan, Y. Qian, *Chem. Mater.* **2015**, *27*, 4156–4164.
- [22] G. Cui, N. Kaskhedikar, J. Maier, L. Gu, P. A. Aken, L. Zhi, K. Müllen, *Adv. Mater.* **2008**, *18*, 20.
- [23] M.-H. Seo, M. Park, K. T. Lee, K. Kim, J. Kim, J. Cho, *Energy Environ. Sci.* **2011**, *4*, 425–428.
- [24] K. H. Seng, M.-H. Park, Z. P. Guo, H. K. Liu, J. Cho, *Angew. Chem. Int. Ed.* **2012**, *23*, 5755–5759.

- [25] J. Liu, K. Song, C. Zhu, C. C. Chen, P. A. van Aken, J. Maier, Y. Yu, *ACS Nano* **2014**, *8*, 7051–7059.
- [26] D. T. Ngo, R. S. Kalubarme, H. T. T. Le, J. G. Fisher, C.-N. Park, I.-D. Kim, C.-J. Park, *Adv. Funct. Mater.* **2014**, *24*, 5291–5298.
- [27] H. Kim, Y. Son, C. Park, J. Cho, H. C. Choi, *Angew. Chem. Int. Ed.* **2013**, *52*, 5997–6001.
- [28] C. Wang, J. Ju, Y. Yang, Y. Tang, J. Lin, Z. Shi, R. P. S. Han, F. Huang, *J. Mater. Chem. A* **2013**, *1*, 8897–8902.
- [29] J.-G. Ren, Q.-H. Wu, H. Tang, G. Hong, W. Zhang, S.-T. Lee, *J. Mater. Chem. A* **2013**, *1*, 1821–1826.
- [30] C. Zhong, J.-Z. Wang, X.-W. Gao, D. Wexler, H.-K. Liu, *J. Mater. Chem. A* **2013**, *1*, 10798–10804.
- [31] W. Tang, Y. Liu, C. Peng, M. Y. Hu, X. Deng, M. Lin, J. Z. Hu, K. P. Loh, *J. Am. Chem. Soc.* **2015**, *137*, 2600–2607.
- [32] S. Goriparti, U. Gulzar, E. Miele, F. Palazon, A. Scarpellini, S. Marras, S. Monaco, R. P. Zaccaria, C. Capiglia, *J. Mater. Chem. A* **2017**, *5*, 19721–19728.
- [33] X. Qiao, X.-B. Yang, N. Zhang, X.-L. Wang, Y.-Y. Song, Y.-Q. Zhai, D. Li, H.-Q. Wang, *Rare Met.* **2021**, *40*, 2432–2439.
- [34] D. Li, K. H. Seng, D. Shi, Z. Chen, H. K. Liu, Z. Guo, *J. Mater. Chem. A* **2013**, *1*, 14115–14121.
- [35] S. Fang, L. Shen, H. Zheng, X. Zhang, *J. Mater. Chem. A* **2015**, *3*, 1498–1503.
- [36] R. Zhao, Z. Liang, S. Gao, C. Yang, B. Zhu, J. Zhao, C. Qu, R. Zou, Q. Xu, *Angew. Chem. Int. Ed.* **2019**, *58*, 1975–1979.
- [37] K. Lee, S. Choi, S. Park, H. R. Moon, *Chem. Mater.* **2016**, *28*, 4403–4408.

Manuscript received: June 30, 2024

Revised manuscript received: August 27, 2024

Accepted manuscript online: September 4, 2024

Version of record online: October 23, 2024
